GSI

Preprint 2003 – 30
October

Statistical Multifragmentation of Non-Spherical Expanding Sources in Central Heavy-Ion Collisions

A. Le Fèvre, M. Płoszajczak, V.D. Toneev, G. Auger,
M.L. Begemann-Blaich, N. Bellaize, R. Bittiger, F. Bocage,
B. Borderie, R. Bougault, B. Bouriquet, J.L. Charvet, A. Chbihi,
R. Dayras, D. Durand,J.D. Frankland, E. Galichet, D. Gourio,
D. Guinet, S. Hudan, B. Hurst, P. Lautesse, F. Lavaud,
R. Legrain, Q. Lopez, J. Łukasik, U. Lynen, W.F.J. Müller,
L.Nalpas, H. Orth, E. Plagnol, E. Rosato, A. Saija, C. Schwarz,
C. Sfienti, B. Tamain, W. Trautmann, A. Trzciński, K. Turzó,
E. Vient, M. Vigilante, C. Volant, B. Zwieglíński, A.S. Botvina

Gesellschaft für Schwerionenforschung mbH
Planckstraße 1 • D-64291 Darmstadt • Germany
Postfach 11 05 52 • D-64220 Darmstadt • Germany

Statistical Multifragmentation of Non-Spherical Expanding Sources in Central Heavy-Ion Collisions

A. Le Fèvre [a], M. Płoszajczak [b], V.D. Toneev [j], G. Auger [b], M.L. Begemann-Blaich [a], N. Bellaize [d], R. Bittiger [a], F. Bocage [d], B. Borderie [c], R. Bougault [d], B. Bouriquet [b], J.L. Charvet [e], A. Chbihi [b], R. Dayras [e], D. Durand [d], J.D. Frankland [b], E. Galichet [c,ℓ], D. Gourio [a], D. Guinet [f], S. Hudan [b], B. Hurst [d], P. Lautesse [f], F. Lavaud [c], R. Legrain [e,1], O. Lopez [d], J. Łukasik [a,k], U. Lynen [a], W.F.J. Müller [a], L. Nalpas [e], H. Orth [a], E. Plagnol [c], E. Rosato [g], A. Saija [h], C. Schwarz [a], C. Sfienti [a], B. Tamain [d], W. Trautmann [a], A. Trzciński [i], K. Turzó [a], E. Vient [d], M. Vigilante [g], C. Volant [e], B. Zwiegliński [i] and A.S. Botvina [a,m]
(The INDRA and ALADIN Collaborations)

[a] *Gesellschaft für Schwerionenforschung mbH, D-64291 Darmstadt, Germany*

[b] *GANIL, CEA and IN2P3-CNRS, F-14076 Caen, France*

[c] *Institut de Physique Nucléaire, IN2P3-CNRS and University, F-91406 Orsay, France*

[d] *LPC Caen, IN2P3-CNRS, ENSICAEN and University, F-14050 Caen, France*

[e] *DAPNIA/SPhN, CEA/Saclay, F-91191 Gif-sur-Yvette, France*

[f] *Institut de Physique Nucléaire, IN2P3-CNRS and University, F-69622 Villeurbanne, France*

[g] *Dipartimento di Scienze Fisiche e Sezione INFN, Univ. Federico II, I-80126 Napoli, Italy*

[h] *Dipartimento di Fisica dell' Università and INFN, I-95129 Catania, Italy*

[i] *A. Sołtan Institute for Nuclear Studies, Pl-00681 Warsaw, Poland*

[j] *Bogoliubov Laboratory of Theoretical Physics, JINR, Dubna, 141980 Moscow Region, Russia*

[k] *H. Niewodniczański Institute of Nuclear Physics, Pl-31342 Kraków, Poland*

[ℓ] *Conservatoire National des Arts et Métiers, F-75141 Paris Cedex 03, France*

[m] *Institute for Nuclear Research, 117312 Moscow, Russia*

Preprint submitted to Elsevier Science *23 September 2003*

Abstract

We study the anisotropy effects measured with INDRA at GSI in central collisions of ^{129}Xe+^{nat}Sn at 50 A MeV and ^{197}Au+^{197}Au at 60, 80, 100 A MeV incident energy. The microcanonical multifragmentation model with non-spherical sources is used to simulate an incomplete shape relaxation of the multifragmenting system. This model is employed to interpret observed anisotropic distributions in the fragment size and mean kinetic energy. The data can be well reproduced if an expanding prolate source aligned along the beam direction is assumed. In the model, the anisotropy is the result of correlations between the charge of a fragment and its location in the freeze-out configuration, created by the mutual Coulomb interactions inside the non-spherical source. An either non-Hubblean or non-isotropic radial expansion is required to describe the fragment kinetic energies and their anisotropy. The qualitative similarity of the results for the studied reactions suggests that the concept of a longitudinally elongated freeze-out configuration is generally applicable for central collisions of heavy systems. The deformation decreases slightly with increasing beam energy.

Key words: multifragmentation, source shape, statistical model, collective flow
PACS: 25.70.Pq, 24.60.-k, 25.75.Ld

1 Introduction

Numerous transport calculations indicate that in central heavy-ion collisions at intermediate energies significant compression and heating of nuclear matter occur in the initial stage of the reaction (see, e.g., [1,2,3,4]). The expansion of initially hot and compressed matter is thought to result in the development of dynamical instabilities leading to the multifragmentation, i.e. to the formation of a large number of intermediate-mass fragments as it is observed experimentally [5,6]. Traces of the pre-equilibrium processes in the disassembling source and the flow energy initially stored in the compressed mode are expected to appear in the fragmentation patterns. The formed composite system may, in particular, have a non-spherical or even a non-compact configuration which will affect the later stages of the decay process. Such configurations can be the result of a transparency, i.e. of an incomplete stopping of the colliding system, as reported for heavy-ion reactions at intermediate [7,8,9] and high [10] energies. The composite system disintegrates into fragments before complete equilibrium has been attained.

[1] Deceased.

Although the collision dynamics plays an essential role, general features of the multifragmentation process, especially the fragment partitions, have been successfully described using the equilibrium statistical models [11,12]. In these models, the system is allowed to explore the phase space of possible partitions into light particles and fragments within an expanded volume. In their standard versions, a spherical breakup volume is used which causes the fragment distributions to be isotropic. While isotropy has been reported for fragmentations initiated with relativistic projectiles (see, e.g., [13,14,15]) it is not necessarily a generic property of multifragmentation. In the heavy symmetric collision systems at intermediate energies studied in the present work, non-isotropic distributions are found to prevail in central collisions if standard methods are used for their identification [9,16,17,18]. A selection of subclasses of central events that fulfill the demand of isotropic emission patterns requires additional conditions for global event properties or for specific observables [19,20,21,22,23]. The resulting cross sections are rather small.

Angular anisotropies in fragment distributions and kinetic energies are usually considered as an indication for genuine non-equilibrium effects. Indeed, dynamical models are able to account for these anisotropies [9] but it is difficult with these models to assess the degree of equilibration that is otherwise reached at the fragmentation stage of the reaction [24]. In a general statistical description, on the other hand, the shape degrees of freedom of the emitting sources will have to be included [25]. Fluctuations around an average shape and isotropic orientations are expected in the unconstrained case while a preference for non-spherical shapes and non-isotropic orientations may result from dynamical effects. Spherical or near-spherical shapes can still be part of such dynamically constrained ensembles.

In the present paper, starting from the observed characteristics of central collisions, an effective deformation of the expanding fragmenting source is considered as a result of an incomplete shape relaxation. Apart from this dynamical imprint, the system is assumed to have attained equilibrium in all other degrees of freedom. The possibility of collective flow, decoupled from the statistical degrees of freedom, is furthermore included. In statistical analyses for the present and similar systems, an additional collective flow component has been shown to be essential for reproducing the fragment kinetic energies [16,18,20,21,26,27,28]. Customarily, it is superimposed without considering its potential correlation with the partition degree of freedom, an assumption that finds its justification in the successful description of the experimental data that it permits [29].

In this framework, we shall analyze various manifestations of anisotropy in fragment observables from central collisions of ^{129}Xe+^{nat}Sn at 50 A MeV and ^{197}Au+^{197}Au at 60, 80 and 100 A MeV, measured at GSI with the INDRA multidetector. The analysis is performed with the Metropolis Multifragmen-

tation Monte-Carlo (MMMC) model [11] which has been extended to non-spherical (NS) sources [16], a version referred to in the following as MMMC-NS model. The MMMC Statistical Model is based on the microcanonical ensemble and has found wide applications in the multifragmentation regime (see, e.g., [11,30,31]).

The ^{129}Xe+^{nat}Sn reaction has been previously studied at GANIL as part of the first INDRA campaign [9,20,22,32,33,34,35]. Reactions of ^{197}Au+^{197}Au have been studied at lower [19,36,37] as well as at higher ($\geq$ 100 A MeV) incident energies [38,39,40]. The present experiment covers the range 40 to 150 A MeV for ^{197}Au+^{197}Au, and the new results obtained for peripheral collisions have been reported [41,42]. A study of central collisions and their analysis within the statistical multifragmentation model (SMM, Ref. [12]) has been performed by Lavaud *et al.* for the range 40 to 100 A MeV [18,43].

The paper is organized as follows: experimental details and the criteria used for selecting central collisions are presented in Sect. 2. Central collisions of ^{129}Xe+^{nat}Sn at 50 A MeV incident energy are chosen to illustrate the analysis procedure (Sect. 3), and their general characteristics are given in Sect 3.1. Using the MMMC-NS model, we first determine the general properties of the source, its mass and excitation energy (Sect. 3.2), and the strength of the collective radial flow (Sect. 3.3). We then detail the protocol developed to investigate independently the geometrical properties of the source (Sect. 3.4) and the velocity profile of the collective radial flow (Sect. 3.5). Standard event-shape variables are finally used to confirm the validity of the derived conclusions (Sect. 3.6). To investigate the dependence of the anisotropy effects on the mass of the system and on the bombarding energy, we apply the same analysis to the heavier system ^{197}Au+^{197}Au at the similar beam energy 60 A MeV (Sect. 4.1) and at the higher energies 80 and 100 A MeV (Sect. 4.2). Finally, in Sect. 5 we summarize and discuss the main results of the paper.

2 Experimental details and data selection

The experimental data have been obtained during the INDRA campaign performed at the GSI laboratory in 1998 and 1999. Beams of ^{129}Xe and ^{197}Au, delivered by the heavy ion synchrotron SIS were directed onto ^{nat}Sn and Au targets with areal densities of 1.05 mg/cm^2 and 2.0 mg/cm^2, respectively. The reaction products were detected and identified with the 4π multidetector INDRA described in detail in [44,45]. For the present campaign, the first ring of the multidetector, covering the polar angles between 2° and 3°, has been modified in order to improve the energy and charge resolution and to permit the mass identification of light products in the range $Z = 1$ to 4. Without changes of the ring geometry, the previously used phoswich detectors have been re-

placed by 12 Si-CsI(Tl) telescopes, each consisting of a 300-μm Si detector and a 14-cm-long CsI(Tl) scintillator viewed by a photomultiplier. These new detectors have the same characteristics as those used in the neighbouring INDRA rings.

In order to verify that the SIS beams are properly focused into the 12-mm-diameter entrance hole of INDRA, annular plastic detectors were placed upstream of the INDRA detection system, and their signals recorded for vetoing halo events in the off-line analysis. Measurements with empty target frames have also been performed. The event triggering condition was set to a hit multiplicity greater than 2 over all CsI detectors. This was sufficient to exclude elastic scattering and to suppress other background generated by cosmic rays and natural or induced radioactivity near the detectors.

The energy calibration of $Z \leq 2$ particles for the 192 CsI(Tl) detectors of the 9 forward-most rings of INDRA has primarily been derived from a detector-by-detector comparison of spectra obtained in the reaction ^{129}Xe+$^{\rm nat}$Sn at 50 A MeV with those measured for the same reaction at GANIL. There, calibration data had been obtained by scattering a variety of primary and secondary beams from thick targets [46]. The remaining 144 CsI(Tl) detectors of rings 10-17 have been calibrated using the standard method [44] based on the silicon calibration telescopes (one per ring): the spectra of $Z \leq 2$ particles obtained for each scintillator have been adjusted to those measured simultaneously by the telescopes during an experiment. The validity of these calibration procedures has been verified for part of the detector by analyzing the spectra of recoil protons from ^{1}H + ^{12}C scattering, obtained with ^{12}C beams of 30 A MeV and a polyethylene target [47].

In order to calibrate the energies of heavier fragments (from Li to Au) with the use of the calibration parameters obtained for α-particles for all INDRA modules (rings 1-17), the light emission from the CsI(Tl) scintillators has been parameterized according to Ref. [48], and the additional Z dependence of the parameters was obtained by comparing the experimental ΔE-E maps to predictions of the range-energy tables [49].

The total transverse energy $E_{\perp}^{12}$ of light charged particles ($Z \leq 2$) which has been used in previous studies [9,32,34,41] but also the multiplicity $M_{\rm c}$ of charged particles were chosen to select central collisions. Inclusive spectra of these quantities for the reactions ^{129}Xe+$^{\rm nat}$Sn at 50 A MeV and ^{197}Au+^{197}Au at 60 A MeV are shown in Fig. 1. The hatched areas indicate the groups of central collisions accepted in the present analysis. They correspond to 1% of the recorded reaction cross section or to reduced impact parameters $b/b_{\rm max} \leq 0.1$ if a monotonic relation with the impact parameter is assumed. It is obvious, in particular from the $M_{\rm c}$ spectra, that these high thresholds favour the tails of the distributions which may be partly caused by the fluctuation widths of

$E_\perp^{12}$ and M_c in central collisions rather than by a significant variation of the impact parameter up to the highest values of these variables.

The monotonic relation between $E_\perp^{12}$ and the reduced impact parameter b/b_{max} resulting from the geometrical prescription [50] is linear to a good approximation, with b/b_{max} decreasing with increasing $E_\perp^{12}$. This is illustrated in Fig. 2 (left panel) for the system ^{197}Au+^{197}Au at 60 A MeV. The relation between M_c and b/b_{max} for this reaction (Fig. 2, right panel) exhibits a change of slope near $M_c = 40$ beyond which b/b_{max} varies much more rapidly with M_c. A similar behavior is not apparent in the correlation of $E_\perp^{12}$ with b/b_{max}.

The correlation between the two variables $E_\perp^{12}$ and M_c is shown in Fig. 3 for the same two systems ^{129}Xe+^{nat}Sn at 50 A MeV and ^{197}Au+^{197}Au at 60 A MeV. It is linear at small values of these observables, i.e. for peripheral collisions. For the most violent collisions we observe a tendency of M_c to saturate. The multiplicity of intermediate-mass fragments ($Z > 2$), represented by the shadings in the figure, is more strongly correlated with M_c than with $E_\perp^{12}$. For a given total multiplicity M_c or multiplicity of fragments, the fluctuations of $E_\perp^{12}$ are rather large. There is even the indication of a weak anti-correlation between the multiplicity of fragments and $E_\perp^{12}$; the largest number of fragments is observed for the region of largest M_c but, at a given bin of M_c, at the smallest $E_\perp^{12}$. This observation may reflect the fact that the production of fragments is governed by the amount of energy that is left available in the system and, apparently, subject to a competition with the energy used for light-particle emission. The figure, furthermore, shows that the central event classes selected with the two criteria are to a large extent mutually exclusive.

3 Central collisions of ^{129}Xe+^{nat}Sn at 50 A MeV

3.1 General characteristics

The global characteristics of central collisions of ^{129}Xe+^{nat}Sn at 50 A MeV, identified on the basis of either $E_\perp^{12}$ or M_c, are shown in Table 1. They are largely independent of the chosen selection criterion, except for the charged-particle and fragment multiplicities which are higher for the M_c selected event class. The difference of about 20% reflects the autocorrelation introduced by gating on the multiplicity itself (Fig. 3). In order to illustrate the effect of the incomplete acceptance of the detector, the same observables are also evaluated for the subclass of events for which at least 80% of the system charge has been recovered in the form of detected charged particles and fragments (values given in parentheses). This additional condition has a slightly larger effect on the $E_\perp^{12}$ selected than on the M_c selected event class. A high multiplicity of charged

Table 1
Characteristics of central collisions of ^{129}Xe+^{nat}Sn at 50 A MeV, selected by the M_c or $E_\perp^{12}$ cuts, and MMMC-NS predictions with the prolate source adjusted to the $E_\perp^{12}$ selected experimental events (for the source parameters see Table 2). Mean values are given for the observables (from top to bottom) multiplicity M_c of charged particles, multiplicity M_{frag} of fragments with $Z > 2$, the atomic numbers Z_{max} of the largest (Z_{max1}) and of the second and third largest fragments (Z_{max2}, Z_{max3}), sphericity s and coplanarity c (Sect. 3.6), sum ΣZ of the fragment charges, and their kinetic energies ΣE_{kin} in the center of mass (in units of MeV), summed over $Z > 2$ and $Z > 5$. The values in parentheses are obtained for the event class with 80% completeness in charge detection. Using the fact that the system is nearly symmetric, the multiplicities and the sums over charge and kinetic energies are obtained by doubling the mean values obtained for the forward hemisphere ($\theta_{cm} \leq 90°$) where the acceptance for fragments is higher.

Observables	Experiment		MMMC-NS
	$E_\perp^{12}$ selection	M_c selection	
M_c	33 (34)	39 (39)	20 (21)
$M_{frag}(Z > 2)$	5.3 (6.3)	6.5 (6.9)	5.9 (6.6)
Z_{max1}	13.3 (15.6)	12.3 (13.1)	13.7 (15.0)
Z_{max2}	7.4 (9.9)	7.8 (8.5)	8.0 (8.7)
Z_{max3}	4.3 (6.6)	5.4 (6.2)	6.1 (6.6)
s	0.49 (0.53)	0.55 (0.56)	0.56 (0.57)
c	0.15 (0.14)	0.14 (0.14)	0.14 (0.13)
$\Sigma Z(Z > 2)$	39 (50)	42 (46)	44 (50)
$\Sigma E_{kin}(Z > 2)$	400 (491)	418 (456)	407 (468)
$\Sigma E_{kin}(Z > 5)$	252 (336)	256 (292)	256 (305)

particles, $M_c > 30$, and a fraction of about 50% of the system charge bound in fragments characterize this multifragmentation mode. Correspondingly, even the biggest fragments of the partition ($Z_{max1} \approx 12$ to 15) are relatively small, with the next largest fragments rapidly decreasing in charge. The sum of the transverse kinetic energies of charged particles reaches up to 1.0 GeV, of which about two thirds are carried away by light charged particles with $Z \leq 2$ (Fig. 1). This dissipation amounts to about one third of a total of 3.1 GeV incident energy in the center of mass and, even though neutrons and the separation energies are not included, may be taken as a first hint that the projectile is not completely stopped in these most central collisions.

3.2 Global parameters of the statistical source

It is well established for this symmetric reaction that a heavy, hot and expanding composite system is formed in central collisions [9,20,21,22,29,35]. Its properties have been previously determined by requiring the Statistical Multifragmentation Model (SMM, Ref. [12]) to reproduce the partitions and the overall mean kinetic energies of fragments [21]. The obtained source characteristics at freeze-out (at a density of 1/3 of the normal density ρ_0) were a total charge $Z_S = 78$, an excitation energy of 7 A MeV, and a collective radial flow of 2.2 A MeV in addition to the thermal and Coulomb components of the kinetic energies. According to calculations with the BNV transport model [21], these parameters correspond to those of an expanding source in the spinodal region.

This analysis has been repeated with the present data and within the MMMC-NS statistical approach [16]. For this purpose, the code was used in its standard configuration with a spherical source and with the fixed standard value $R = 2.2A^{1/3}$ fm for the freeze-out radius, corresponding to 1/6 of the normal nuclear density [30,51,52]. Collective radial (see below) and angular motions were also included. The chosen angular momentum of 40 $\hbar$, perpendicular to the beam axis, represents an upper limit for this reaction for the lowest range of impact parameters [53]. The correlation function in the relative azimuthal angle between alpha particles is flat (Fig. 4), indicating that the transfer of angular momentum to the formed composite system is too small to permit a pronounced reaction plane to be discerned [54]. In the MMMC-NS calculations, the inclusion of 40 $\hbar$ angular momentum does not significantly alter the fragment partitions, kinetic energies or angular distributions. The calculated alpha-particle correlation function remains also flat in accordance with the measurement (Fig. 4).

In all comparisons with the experimental data, the produced MMMC-NS events have been filtered using a software replica of the experimental apparatus. It takes into account the major properties of the INDRA multidetector, i.e. the geometrical acceptance and the energy thresholds and high-energy cutoffs. In addition, the effects of the multihit treatment in the off-line analysis, based on consistency tests of the recorded ΔE and E signals (so-called coherency), are also simulated. Applying this filtering procedure to the MMMC-NS generated events, acceptances of $\approx 80\%$ and $\approx 70\%$ for fragments ($Z > 2$) and light charged particles ($Z = 1, 2$) were obtained, respectively. They are caused by the geometrical acceptance of INDRA ($\approx 90\%$), by thresholds, and by multihits that cannot be resolved with the coherency analysis, in the majority multihits of light charged particles in a single detector module. Accordingly, the fragment multiplicity ($Z > 2$) for $E_{\perp}^{12}$ selected central events, corrected for instrumental effects, is 6.6 (> 6.9 for 80% completeness, cf. Table 1).

The source parameters were determined by adjusting the calculations in a step-wise procedure to the measured mean characteristics of the fragment partitions. The obtained results were found to be independent of whether the additional condition of 80% charge detection, in both data and filtered calculations, had been requested. In a first step, the excitation energy of the source, $E^* = 6.0$ A MeV, has been determined by requiring the mean value of the largest fragment charge Z_{max1} of the event to be reproduced. This can be done independently of the mass of the source since E^* depends mainly on Z_{max1} and is only weakly sensitive to the total charge of the source Z_{S} (Fig. 5, left panel). This excitation energy corresponds to a mean thermodynamical temperature $T = 5.6$ MeV. In a second step, with E^* being fixed, the source charge Z_{S} is determined by adjusting the total detected charge of fragments $\Sigma Z(Z > 2)$ to its experimental mean value. This observable depends strongly on both the source mass and the excitation energy (Fig. 5, middle panel). For $E^* = 6.0$ A MeV, a value $Z_{\mathrm{S}} = 79$ is obtained for the charge of the equilibrium source of fragments. The assumption that the mean N/Z ratio of the colliding nuclei is preserved yields $A_{\mathrm{S}} = 188$ for the mass. These values correspond to 76% of the total system. The simulations performed in Ref. [16] for an excited gold nucleus with $Z_{\mathrm{S}} = 79$ and $A_{\mathrm{S}} = 197$ yield practically identical results for the observables studied here, in spite of the larger neutron number. The resulting charge distribution of fragments ($Z > 2$) reproduces well the experimental data (Fig. 5, right panel). The difference observed for light particles ($Z \leq 2$) is presumably caused by pre-equilibrium emissions during early phases of the reaction (cf. Sec. 3.4).

While the system mass obtained from the MMMC analysis agrees with the SMM estimate [21], the excitation energy is slightly lower. This can at least partly be traced back to the freeze-out volume which in the MMMC-NS model has twice the value used in the SMM. The Coulomb energy is correspondingly lower, by about 0.8 A MeV for the present system, so that the thermal components of the excitation energy which determine the fragment partitions are about equal.

3.3 Collective radial flow

A collective radial flow of the constituents of the source was incorporated into the MMMC-NS code with the parameterization

$$\vec{v}_{coll}(\vec{r}) = V_{coll}\left(\frac{r}{R_0}\right)^{\alpha_{coll}}\left(\frac{\vec{r}}{r}\right) \qquad (1)$$

where $\vec{r}$ is the position vector in coordinate space with respect to the center of mass, and V_{coll}, R_0 and α_{coll} denote the strength, the scaling radius and the

exponent of the flow profile, respectively. R_0 is set to be equal to the radius of the system at normal density. To obtain satisfactory descriptions of the observed anisotropies, it was found necessary to either permit $\alpha_{\rm coll}$ to differ from unity, i.e. to deviate from the standard Hubblean self-similar flow profile [16,28,55], or to consider non-isotropic strength parameters $V_{\rm coll}(\theta_{\rm cm})$ [18,43]. The collective energy is not included in the energy balance, and the flow is thus decoupled from the equilibrium. This assumption is justified in a quasi-static-expansion approximation in which the expansion is slow as compared to the equilibration time.

The strength parameter $V_{\rm coll}$ is determined from the requirement that the sum of the kinetic energies of fragments with $Z > 5$, $\Sigma E_{\rm kin}(Z > 5)$ as given in Table 1, is reproduced. In the cases with isotropic $V_{\rm coll}$, a flow exponent $\alpha_{\rm coll} = 2$ has been used since the observed anisotropies in momentum space are best accounted for with this value (Sect. 3.5). This is not crucial for the spherical source for which the result for $V_{\rm coll}$ is nearly independent of the choice made for $\alpha_{\rm coll}$, a consequence of the specific parameterization Eq. 1 and the chosen scaling radius R_0. The obtained value $V_{\rm coll} = 0.07c$ corresponds to a mean collective energy $< E_{\rm coll} > = 2.4$ A MeV. This result is close to the values 2.2 A MeV from the SMM analysis [21] and 2.0 A MeV obtained with the phenomenological model used in [20]. The spherical-source characteristics are summarized in Table 2.

From the sum of the collective energy and the thermal excitation energy, we deduce a total excitation energy of 8.4 A MeV at freeze-out. This value is considerably smaller than the 12 A MeV that have been extracted experimentally for a small subset of central collisions of the same system with a calorimetric method [20]. A difference of several MeV per nucleon between the excitation energies needed to describe the fragmentation within statistical models and those deduced from summing up the breakup Q-values and kinetic energies has also been observed for other types of reactions and ascribed to preequilibrium emissions [13]. Also in the present case the emission of light charged particles is underestimated by the MMMC model (Table 1 and Fig. 5, right panel). Part of the difference may also be caused by the selection of a specific event sample with high sphericity that was chosen in [20].

The global event-shape observables sphericity and coplanarity, deduced from the three-dimensional tensor of fragment momenta [56] and discussed in detail in Sect. 3.6, are included in Table 1. The experimental mean sphericity determined for the $E_{\perp}^{12}$ selected event class is $< s > = 0.49$ and, thus, considerably smaller than the prediction $< s > = 0.71$ obtained, after filtering, with the MMMC-NS code in the spherical-source limit (note that the limiting values $< s > = 1.0$ and $< c > = 0.0$ cannot be reached with a finite number of fragments). The coplanarity is small which, for non-spherical shapes, is expected for prolate deformations with approximately azimuthal symme-

Table 2
Source characteristics for ^{129}Xe+^{nat}Sn at 50 A MeV used in the MMMC-NS calculations: charge Z_S, mass A_S and excitation energy E^* of the source, transversal-to-longitudinal elongation $\mathcal{R}$ in coordinate space, collective radial flow parameters V_{coll} (strength) and α_{coll} (exponent), and resulting mean kinetic energy of the radial flow. The elongation of the ellipsoidal flow in velocity space is 0.30:1 and 0.70:1 for the spherical (Sphere+e.f.) and prolate (Prolate+e.f.) sources, respectively. In all cases, the angular momentum perpendicular to the beam axis is 40 $\hbar$, and the reduced freeze-out radius is $r_0 = 2.2$ fm.

Source shape	Prolate	Sphere	Oblate	Sphere+e.f.	Prolate+e.f.
Z_S	79	79	79	79	79
A_S	188	188	188	188	188
E^* (A MeV)	6.0	6.0	6.0	6.0	6.0
$\mathcal{R}$	0.70:1	1:1	1.67 : 1	1:1	0.70:1
V_{coll} (c)	0.06	0.07	0.05	0.07	0.06
α_{coll}	2	2	2	1	1
$< E_{coll} >$ (A MeV)	2.3	2.4	1.8	1.9	2.1

try. The spherical-source model, while adequately accounting for the partition degrees of freedom, cannot reproduce the source shape in momentum space. As will be shown in the following, the indicated prolate source deformation is confirmed by the results obtained for other observables which reflect the angular dependence of the masses and the kinetic energies of the fragments. These anisotropies indicate that the system has not completely relaxed and that part of its total energy is bound in other degrees of freedom and, hence, not available for the thermal equilibration.

3.4 Anisotropy of heavy-fragment distribution and the spatial elongation of the source

In the MMMC-NS statistical approach [16], the fragment partitions are accomodated within a given source volume. Besides the spherical shape, also prolate and oblate source geometries are included here, i.e. elongated and compressed ellipsoids in coordinate space, aligned with respect to the beam axis. These three kinds of sources are meant to represent possible dynamical scenarios for the source formation prior to freeze-out. For the spherical and prolate sources, besides isotropic radial flow, also the possibility of ellipsoidal radial flow is considered. It is generated by weighting the parameter V_{coll} (Eq. 1) with a geometrical function that describes an ellipsoid in momentum space elongated along the beam axis. The deformation is adjusted so as to reproduce the experimental angular dependence of the fragment kinetic

energies (see Sect. 3.5).

We shall now analyze various observables related to the charge distributions and anisotropies and test their sensitivity to the source elongation in coordinate space. The charge of the largest fragment of a partition has a mean value $\langle Z_{\mathrm{max1}} \rangle = 15.6$ (Table 1) but is on average $\approx 20\%$ smaller if the heaviest fragments are emitted sidewards ($\theta_{\mathrm{cm}} \approx 90°$) than when they are emitted in forward or backward directions (Fig. 6). Already this first experimental observation can only be reproduced with the assumption of a prolate source shape but not with any of the other alternatives. The best fit to the data is obtained with a spatial elongation given by the transversal-to-longitudinal ratio $\mathcal{R} = 0.70 : 1$, determined with a statistical accuracy of $\pm 3\%$. This corresponds to a deformation parameter [57]

$$\delta = \frac{3}{2} \frac{1 - \mathcal{R}^2}{1 + 2\mathcal{R}^2} = 0.386$$

which, for comparison, is of the same order as what is found for many deformed nuclei in the rare-earth region. In the following, the elongation of the prolate source will be kept fixed. For the oblate source, further used for illustration purposes, an elongation 1.67:1 has been arbitrarily chosen. Moderate deformations of this magnitude do not significantly modify the partitions. Vice versa, the global source parameters mass, excitation energy and the strength of the collective flow, as determined for the various types of sources, are approximately the same (Table 2).

The angular anisotropy is also apparent in the yield distributions as a function of the fragment atomic number Z (Fig. 7). More and larger fragments are produced in the forward region (polar angle $\theta_{\mathrm{cm}} \leq 60°$) than at sideward directions ($60° < \theta_{\mathrm{cm}} \leq 120°$), with a relative difference that increases with Z. For central events selected on the basis of M_{c}, the effect remains but the multiplicities are slightly lower for large Z. On the other hand, the multiplicities for $Z \leq 2$ in the forward direction are larger, presumably due to light particles emitted during the pre-equilibrium phases of the reaction. In contrast, with the $E_{\perp}^{12}$ selection, the sideward multiplicities of light particles increase noticeably and become equal to the forward multiplicities. This is obviously an auto-correlation produced by the selection method. Comparing the experimental multiplicities for $Z \leq 2$ to the MMMC-NS calculation which are supposed to account for the equilibrium phase only, we conclude that nearly half of the measured light charged particles originate from either the early pre-equilibrium stage or from the expansion of the composite system prior to breakup (Fig. 7 and Table 1).

As demonstrated in Fig. 7, the simulation with the prolate source reproduces the experimental forward-sideward difference in fragment yields. The spherical

source model produces no angular dependence, as expected, whereas the oblate source predicts an opposite trend with smaller yields in forward and backward directions. Another observable with a strong shape discrimination power is the angular distribution of the largest fragment (Fig. 8). Again, a strong forward-backward focusing is observed and only the MMMC-NS prolate source can describe it. The spherical source with isotropic flow yields a flat distribution but with a weak slope caused by the simulated INDRA acceptance. The superposition of a non-isotropic collective flow does not significantly modify this result because of the radial nature of the flow and because of the small magnitude required in the present case. A non-isotropic flow, therefore, cannot simulate the effects of a spatial source deformation on the observables studied so far.

In the MMMC-NS prolate simulation, the strong forward-backward focusing of the heaviest fragments originates from their particular location in the freeze-out volume. This is a consequence of the minimization of the Coulomb energy on an event-by-event basis which favours a concentration of large fragments near the tips of the source and reduces the weight of partitions with high Coulomb energy, as, e.g., with heavy fragments compactly distributed near the center of the freeze-out volume. As illustrated in Fig. 9 (middle panels), the transversal and longitudinal projections of the yields of heavy fragments ($Z > 4$) for slices in the coordinate space show that the interior of the source is strongly depleted. Heavy fragments are emitted predominantly from the tips of the ellipsoid close to the surface. This focusing is enhanced for larger fragment charges but is absent for light charged particles. Since the radial collective flow is directly correlated with the spatial fragment distribution (see Eq. 1), the geometry of the source and its ring structure in the transversal cut are reflected in the velocity space, as shown in the right panels of Fig. 9. Depending on the relative strengths of the thermal and collective components, this space-momentum correlation is partly smeared out by thermal motion.

An illustration of the decisive role of the Coulomb energy is given in the left panels of Fig. 9. If the Coulomb interaction is artificially switched off, heavy fragments are found to be much more homogeneously spread over the freeze-out volume. There is still a slight concentration near the surface, caused by the geometrical advantage it gives for placing the other fragments of the partition. In this case, the resulting angular distribution of heavy fragments becomes much flatter and does no longer agree with the experimental observation.

3.5 Kinetic energies and the anisotropy of the collective flow

The collective motion is not included in the energy balance of the MMMC-NS model. Therefore, the yield and charge distributions primarily discussed up to

now are only weakly dependent on the strength of the included flow (via the applied filter). Because of the radial form of the velocity profile (Eq. 1), also the fragment emission into a given angular interval and the fragment angular distribution are hardly affected. This is no longer valid if the fragment kinetic energies are considered since they depend directly on the strength of the considered flow. The observed anisotropies of the kinetic energy distributions may be accounted for with either an angle-dependent strength parameter $V_{\rm coll}(\theta_{\rm cm})$ or, for a non-spherical source, also by adjusting the exponent $\alpha_{\rm coll}$.

The latter statement is illustrated in Fig. 10 (left and middle panels). The calculated mean kinetic energy as a function of Z for the forward and sideward angular regions depends significantly on the exponent $\alpha_{\rm coll}$ of the velocity profile while the angle-independent $V_{\rm coll}$, adjusted to reproduce the experimental $\Sigma E_{\rm kin}(Z > 5)$, varies little with $\alpha_{\rm coll}$. The anisotropy of the kinetic energy, caused by the source elongation, is strongly enhanced with larger $\alpha_{\rm coll}$. The same property is also reflected by the angular dependence of the mean kinetic energy of the largest fragments (Fig. 10, right panel). In the model description, these fragments are mostly placed far from the center of the source and, therefore, have the highest sensitivity to the exponent of the flow profile. The MMMC-NS prolate simulation gives the best agreement with the experimental data for $\alpha_{\rm coll} = 2.0 \pm 0.2$ (statistical uncertainty). The sensitivity of $E_{\rm kin}(Z)$ to $\alpha_{\rm coll}$ is very high as shown in Fig. 10. The difference between forward and sideward kinetic energies for fragments with, e.g., $Z = 20$ is ≈ 75 MeV in the experiment and for $\alpha_{\rm coll} = 2$ but only 50 MeV and 25 MeV for $\alpha_{\rm coll} = 1$ and 0.5, respectively.

Naturally, the forward-backward enhancement of the kinetic energies may also be very satisfactorily accounted for with a non-isotropic strength parameter. For ^{129}Xe+$^{\rm nat}$Sn at 50 A MeV, the present analysis with the spherical MMMC source requires a large elongation of 0.3:1 (Table 2, Spherical+e.f.). With a slightly different procedure based on the SMM, this has also been demonstrated by Lavaud *et al.* for the ^{197}Au+^{197}Au data from the present experiment [18,43]. The required effective elongation in velocity space ranges from ≈ 0.5:1 for ^{197}Au+^{197}Au at 40 A MeV to ≈ 0.7:1 for the same reaction at 100 A MeV incident energy. For the prolate MMMC-NS source and ^{129}Xe+$^{\rm nat}$Sn at 50 A MeV, the required elongation in velocity space is smaller, as expected. With the same source elongation 0.70:1 that was obtained for the coordinate space (Table 2, Prolate+e.f.), an equivalent reproduction of the kinetic energies is obtained, even though the values for the largest Z may be slightly overpredicted (Fig. 11). This coincidence is interesting as it permits the source deformation to be explained rather naturally as resulting from a non-isotropic collective expansion.

The collective flow, on average, provides more than half of the fragment kinetic energy. It is then not surprising that the flow parameterization influences

significantly also the shape of the energy spectra. This is illustrated in Fig. 12 where the measured kinetic energy spectra of fragments with $Z = 6$ and 10 are compared with the MMMC-NS prolate predictions for isotropic $V_{\rm coll}$ and variable $\alpha_{\rm coll}$. There is little sensitivity to $\alpha_{\rm coll}$ at sideward angles but, at the forward angles, the shapes of the experimental spectra are only reproduced with $\alpha_{\rm coll} \approx 2$. At these angles of maximal spatial extension of the source, a velocity profile with $\alpha_{\rm coll} = 2$ results in broader spectra and higher kinetic energies than obtained with the standard Hubblean profile.

3.6 Global event-shape observables

In order to confirm the spatial and flow properties of the prolate source, predicted by the MMMC-NS model and determined in the preceding sections, we shall now study the global event-shape observables sphericity s, coplanarity c and flow angle $\Theta_{\rm flow}$ which refer to the event shape in momentum space.

Following Ref. [56], we perform the event-by-event global analysis based on the three-dimensional momentum tensor, calculated in the center of mass of the reaction:

$$Q_{ij} = \sum_{\nu=1}^{N} \frac{1}{2m_{(\nu)}} \; p_i^{(\nu)} \, p_j^{(\nu)} \quad , \tag{2}$$

where $p_i^{(\nu)}$ is the i-th Cartesian coordinate ($i = 1, 2, 3$) of the center-of-mass momentum $p^{(\nu)}$ of the fragment ν with the mass $m_{(\nu)}$. With the chosen weighting $1/2m_{(\nu)}$, it represents the kinetic energy flow within the event. To reduce the effects of secondary decay and of pre-equilibrium particle emission, the light charged particles are excluded and the sum in Eq. 2 is taken only over fragments with $Z \geq 3$. The tensor Q_{ij} can be represented as an ellipsoid to be described by three axes and by an orientation defined by three angles in the three-dimensional momentum space. This is usually done by referring to the eigenvalues $0 \leq \lambda_1 \leq \lambda_2 \leq \lambda_3$ of the tensor Q_{ij}, with the normalization $\lambda_1 + \lambda_2 + \lambda_3 = 1$, and to the Euler angles defining the eigenvectors $\vec{e}_1, \vec{e}_2, \vec{e}_3$. From various possible combinations of these parameters defining global variables [56], we consider here the sphericity, $s = (3/2)(1 - \lambda_3)$, which varies from 0 for a pencil-like event to 1 for a spherically symmetric event, the coplanarity, $c = (\sqrt{3}/2)(\lambda_2 - \lambda_1)$, which extends from 0 (for spherical or pencil-like configurations) to $\sqrt{3}/4$ (for a disk), and the flow angle $\Theta_{\rm flow}$ defined as the angle between $\vec{e}_3$ and the z-direction (the beam direction). The flow angle is most useful for prolate shapes for which it describes the degree of alignment with respect to the beam axis ($\Theta_{\rm flow} = 0°$ for complete alignment).

Although these event-shape variables cannot be used to determine indepen-

dently the source elongation and the flow profile, they can help us to confirm our finding with respect to the source parameters. First, looking at the mean values of the sphericity and coplanarity given in Table 1, we observe a good agreement between the experimental data and the MMMC-NS prolate simulation. Considering now the s and c distributions, depicted in Fig. 13, we note that the agreement with the experiment is remarkable. For comparison, other MMMC-NS shape configurations are included. By construction, the coplanarity distribution allows to exclude an oblate source only and does not discriminate between a spherical form and a prolate one: both give close values of the coplanarity c. On the other hand, the sphericity distribution can exclude all shapes except the prolate one. This is valid even for the spherical shape with non-isotropic flow, even though the latter properly describes the kinetic-energy anisotropy. A similar analysis for different values of the exponent of the flow profile, presented for the prolate shape in Fig. 14, confirms that $\alpha_{\rm coll} = 2$ best describes the distributions of fragment momenta in the present reaction. The parameter $\alpha_{\rm coll}$ has quite a strong effect on the sphericity distribution, because it enhances (for $\alpha_{\rm coll} > 1$) or reduces (for $\alpha_{\rm coll} < 1$) the elongation of a system in the momentum space, as compared to the standard Hubblean radial flow. In contrast, as expected, $\alpha_{\rm coll}$ influences only weakly the coplanarity which measures the azimuthal asymmetries of the prolate events.

A similar comparison has been done for the flow angle distribution (Fig. 15). It is strongly concentrated at small angles, corresponding to the forward-backward enhancement of heavy fragments (Fig. 8) which contribute with large weights to the momentum tensor. This behavior is correctly described only by the MMMC-NS prolate simulation. The yield at high $\Theta_{\rm flow}$ is slightly too low but can be expected to increase if fluctuations around the mean source deformation are included. The spherical configuration with anisotropic flow also reproduces the general trend but the agreement with the experiment is only qualitative. Like in the experimental data, MMMC-NS prolate simulations produce, with a small probability, events having high values of $\Theta_{\rm flow}$. They correspond to rare partitions with the heaviest fragment being emitted sidewards or to compact arrangements of fragments with near-spherical energy-flow distributions. The comparison of the experimental data and the MMMC-NS prolate predictions for various values of $\alpha_{\rm coll}$ is shown in Fig. 15 (right panel). The sensitivity to $\alpha_{\rm coll}$ is not very strong but the general trend that the forward-backward focusing of the momentum tensor increases with $\alpha_{\rm coll}$ can, nevertheless, be clearly seen.

4 Application to a heavier system

4.1 $^{197}Au+^{197}Au$ *at 60 A MeV*

Given the possibility that the forward-backward enhancement observed for the fragment emission in ^{129}Xe+^{nat}Sn might be related to a lack of mutual stopping of the collision partners, an investigation of the mass dependence seems strongly suggested. A more efficient stopping may result from the larger nuclear radii and masses in even heavier systems. The present study has, therefore, been extended to the ^{197}Au+^{197}Au system at the similar beam energy of 60 A MeV that was measured as part of the same experimental campaign of INDRA at GSI [18,43].

The same methods were used for selecting central event samples ($b/b_{max} \leq 0.1$) according to either $E_{\perp}^{12}$ or M_c (cf. Sect. 2), and their mean global characteristics were determined. They are listed in Table 3. As in the ^{129}Xe+^{nat}Sn case, the reaction channels are highly fragmented with multiplicities that, apparently, scale with the mass ratio 1.6 of the two systems. Accordingly, the mean charge $\langle Z_{max1} \rangle$ of the largest fragment of a partition is nearly the same as for ^{129}Xe+^{nat}Sn, and the next largest fragments have also very similar mean charges. The mean sphericity $\langle s \rangle = 0.66$ for ^{197}Au+^{197}Au is larger than the corresponding value $\langle s \rangle = 0.53$ for ^{129}Xe+^{nat}Sn. As it turns out, however, this difference is not connected to a more compact source configuration for the heavier ^{197}Au+^{197}Au system but rather to the larger fragment multiplicities observed in this reaction. The calculated value $\langle s \rangle = 0.67$ (after filtering, Table 3) is obtained with a MMMC-NS source with elongation 0.70:1, identical to that derived for ^{129}Xe+^{nat}Sn at 50 A MeV.

The same analysis protocol as for ^{129}Xe+^{nat}Sn was followed to determine the parameters of the equivalent MMMC-NS source, its charge and mass, the excitation energy (from the charge partitions), and the strength of the collective flow (from $\Sigma E_{kin}(Z > 5)$). Subsequently, the spatial source deformation was derived from the fragment-charge anisotropy, and the exponent α_{coll} adjusted to the anisotropy observed for the fragment kinetic energies. The agreement obtained for the mean characteristics of this reaction in comparison with the experimental data is very satisfactory (Table 3). Only the charged-particle multiplicity is again underpredicted as preequilibrium emissions are not accounted for. The deduced parameters are listed in Table 4. Obviously, to describe central collisions of ^{197}Au+^{197}Au at 60 A MeV, a prolate source is required that is larger, roughly in proportion to the initial masses, but otherwise very similar to the source deduced for ^{129}Xe+^{nat}Sn.

The achieved description of the experimental Z and Z_{max1} distributions and

Table 3
Mean characteristics of central ^{197}Au+^{197}Au collisions at 60 A MeV and the MMMC-NS model predictions for the prolate source with parameters determined from the comparison with the experimental data and listed in Table 4. The presentation is the same as in Table 1.

Observables	Experiment		MMMC-NS
	$E_{\perp}^{12}$ selection	M_c selection	
M_c	50 (53)	56 (55)	33 (34)
M_{frag}	9.3 (10.9)	11.0 (11.9)	10.2 (11.3)
Z_{max1}	13.7 (16.1)	13.3 (14.9)	14.4 (15.7)
Z_{max2}	9.4 (11.8)	9.4 (10.7)	9.4 (10.1)
Z_{max3}	6.9 (9.3)	7.2 (8.4)	7.5 (8.1)
s	0.63 (0.66)	0.65 (0.66)	0.66 (0.67)
c	0.13 (0.12)	0.12 (0.12)	0.12 (0.11)
$\Sigma Z(Z>2)$	62 (79)	68 (78)	66 (75)
$\Sigma E_{kin}(Z>2)$	994 (1168)	1138 (1273)	875 (994)
$\Sigma E_{kin}(Z>5)$	586 (777)	627 (764)	577 (718)

anisotropies is illustrated in Fig. 16. The larger fragment yields at forward angles require the MMMC-NS source to be elongated in coordinate space. The observed anisotropy of the kinetic-energy distribution as a function of Z and for the largest fragment as a function of angle are shown in Fig. 17. Also here a rather satisfactory agreement is obtained. In contrast to ^{129}Xe+^{nat}Sn, a smaller flow exponent ($\alpha_{coll} = 1.5$) seems to be sufficient to account for the anisotropies in the isotropic non-Hubblean flow parameterization (Fig. 17, right panel).

4.2 ^{197}Au+^{197}Au at 80 and 100 A MeV

To extend the present analysis to energies beyond the Fermi energy domain is again of interest because the increasing phase space for Pauli-allowed nucleon-nucleon collisions might enhance the mutual stopping of the colliding ions. The data measured in the same experiment for the ^{197}Au+^{197}Au system at the higher energies 80 and 100 A MeV are, in fact, supportive of such an interpretation. The anisotropies of the fragment yields and energy distributions are slightly lower at the highest bombarding energy. The dominating effects, however, are the rapid increase of the collective component of the fragment kinetic energy and the decreasing slopes in the fragment Z distributions, known from the work of Lavaud *et al.* [18,43] and shown to continue to much higher

Table 4
Incident energy E/A, collision energy in the center-of-mass system E_{cm}/A for the four studied reactions and characteristics of the prolate freeze-out source in central collisions as obtained with the MMMC-NS model. The ^{129}Xe+^{nat}Sn result of Table 2 is included for easier comparison.

Reaction	^{129}Xe+^{nat}Sn	^{197}Au+^{197}Au		
E/A (MeV)	50	60	80	100
E_{cm}/A (MeV)	13.4	14.9	19.8	24.7
Z_S	79 (76%)	125 (79%)	110 (70%)	95 (60%)
A_S	188	312	275	238
E^* (A MeV)	6.0	6.0	6.7	7.3
$\mathcal{R}$	0.70:1	0.70:1	0.70:1	0.76:1
V_{coll} (c)	0.06	0.07	0.095	0.12
α_{coll}	2.0	1.5	1.3	1.2
$< E_{coll} >$ (A MeV)	2.3	3.1	5.2	7.4

bombarding energies by the FOPI Collaboration [40].

The obtained source parameters are listed in Table 4 and compared to those obtained at 60 A MeV for ^{197}Au+^{197}Au and at 50 A MeV for the ^{129}Xe+^{nat}Sn system. The charge of the source decreases slowly with rising beam energy, reflecting the decreasing part of the system that is emitted in the form of bound fragments. The required thermal excitation energy rises slowly (by $\approx$ 20%) while the collective energy increases rapidly, about twice as fast as the available center-of-mass energy. The two quantities become approximately equal at a beam energy of 100 A MeV (Fig. 18). The elongation of the source, on the other hand, remains remarkably stable with the system mass in the energy range between 50 A MeV and 80 A MeV. At 100 A MeV, the source seems to become slightly more compact.

The anisotropy of the fragment kinetic energies decreases simultaneously with a comparably slow pace. For the prolate source with isotropic flow, this appears in the form of a gradual decrease of the required flow exponent to $\alpha_{coll} = 1.2 \pm 0.1$ at 100 A MeV (Table 4). For the spherical SMM source with ellipsoidal flow, the elongation in velocity space decreases from 0.5:1 to 0.7:1 [18,43]. A very satisfactory agreement is also obtained with the parameterization of the prolate MMMC-NS source and ellipsoidal flow if the smaller elongation $\mathcal{R} = 0.76 : 1$ in coordinate space, required at 100 A MeV, is also chosen for the collective velocities. This is illustrated in Fig. 19, the kinetic energies for large Z are again slightly overestimated (cf. Fig. 11).

5 Summary and discussion.

Angular anisotropies in the distributions of fragment size, fragment yield and fragment kinetic energy from multifragmentation in central ^{129}Xe+^{nat}Sn and ^{197}Au+^{197}Au collisions have been measured with INDRA at GSI. The deformation extent of the phase-space available for the composite system at freeze-out, i.e. the spatial source elongation and the parameters of the collective flow, have been extracted from the experimental data by means of the MMMC-NS model. A good description is obtained with a prolate source shape in coordinate space, oriented along the beam axis, and with an additional collective radial flow, superimposed on the thermal and Coulomb velocity components. With the usual assumption of an expanding spherical source the observed anisotropies cannot be explained. The additional assumption of a non-isotropic flow distribution can account for the anisotropies of the kinetic energies but not for those of the fragment charge distributions. The anisotropy of the fragment kinetic energies requires non-Hubblean flow profiles if an isotropic parameterization of the collective velocity component is chosen, in particular for the lower part of the studied range of bombarding energies. The magnitude of the flow increases rapidly with the beam energies and, for the heavier ^{197}Au+^{197}Au system at 100 A MeV, assumes a nearly Hubblean profile.

An important role in the present statistical approach is played by the Coulomb interaction which produces the anisotropies of the fragment yield distributions. Under the constraint of total energy conservation, the position-dependent mutual Coulomb energies induce spatial correlations between the fragments. The superimposed radial flow transforms these spatial fragment-fragment correlations into correlations in their relative velocities. The heaviest fragments of the partition were found to be a most sensitive probe of this scenario. This source of correlations contained in the individual fragment locations is lost if only the average Coulomb energy for a given partition is considered, as in the Wigner-Seitz approximation used in standard versions of statistical multifragmentation models [12]. Coulomb induced spatial anisotropies are considered, besides in the MMMC, also in recent versions of the SMM model and found to be important in peripheral reactions of symmetric systems [58].

Studying the influence of the system mass and beam energy, we have observed that both ^{129}Xe+^{nat}Sn and ^{197}Au+^{197}Au systems behave rather similarly. With increasing beam energy, the equilibrated fragment source represents a decreasing fraction of the mass and charge of the collision system but maintains approximately the same prolate elongation oriented along the beam direction. At the highest energy of 100 A MeV, in the ^{197}Au+^{197}Au system, the source elongation seems to be reduced. Interpreted as a result of the dynamics of the initial reaction stage, it may indicate a more efficient mutual stopping of the colliding heavy ions with increasing beam energy.

At the lower bombarding energies 50 and 60 A MeV, the collective energy of $\approx$ 2 A MeV constitutes only a small fraction of the total energy stored in the decaying system. It is, nevertheless, indispensable if the fragment kinetic energies are to be accounted for. Its magnitude has been deduced rather consistently for various reactions in this energy range and with different methods [5,20,21,27]. The increase of the equilibrated excitation energy $< E^* >$ of the source with increasing beam energy is rather small. In contrast, the collective flow energy $< E_{coll} >$ grows rapidly and becomes equal to the equilibrated energy at 100 A MeV. It seems surprising that, even then, the complete decoupling of the statistical breakup from the collective fragment motion should still be a viable assumption. It has been demonstrated that collective flow affects the partitioning of the system, in particular the survival probability for heavier fragments drops rapidly with increasing flow [59,60,61,62,63]. On the other hand, as shown in several of these references, the effect of the flow on the charge distributions may be simulated by increasing the value of the thermalized energy in the model description [60,63]. It is therefore quite likely that the flow effect is implicitly included in the parameters of the statistical description. At moderate flow values, the changes are expected to be very small [62,63].

A completely orthogonal approach to the question of the coexistence of equilibrated partitions and collective motion has recently been presented by Campi *et al.* [64]. Using classical molecular dynamics calculations and specific clustering algorithms, these authors find fragments to be preformed at the beginning of the expansion stage when the temperature and density are still high. The fragment charge distributions, reflecting the equilibrium at this early stage when the flow is still small, remain nearly unmodified down to the freeze-out density at which the flow has fully developed. While the initial compression density determines the collective flow observed asymptotically, the partitions are governed only by the initial system mass and its internal excitation energy. A fragment preformation at an early stage of the collision has been previously suggested also by other authors [24,65,66,67,68].

Isotropic self-similar flow parameterizations were not found sufficient for the adequate description of the kinetic energies. Either a non-Hubblean radial expansion with $\alpha_{\rm coll} > 1$ or a non-isotropic strength distribution had to be considered, in particular in the range of lower bombarding energies. In ultra-relativistic heavy ion collisions, expansion velocity profiles with $\alpha_{\rm coll} \simeq 2$ have been proposed to explain the transverse flow of hadrons in a blast scenario [69]. For the present regime, a microscopic explanation of this effect within the nonlocal BUU transport model has been proposed by Morawetz *et al.* and also identified as a surface effect [55]. Even a decrease of the collective exponent with bombarding energy is predicted, in qualitative agreement with the present measurement. On the other hand, the need for $\alpha_{\rm coll} > 1$ in the present case arises mainly from the large effect it has on the velocities of the heaviest

fragments which, in the MMMC-NS model, are placed at large distances from the center of the fragmenting source. In a dynamical scenario, these fragments would seem more likely to arise from colder parts of the residual projectile and target matter with incomplete dissipation of their initial energies, rather than from the rapid expansion of a surface shell. This does not reduce the importance of $\alpha_{\rm coll} \neq 1$ for successful parameterizations of the fragment distributions and anisotropies (cf. Ref. [28]).

The anisotropy of the fragment kinetic energies has been equivalently well reproduced with an ellipsoidal flow distribution whose deformation was chosen equal to the prolate source deformation in coordinate space. In an expansion scenario with a (non-isotropic) self-similar velocity profile, the shape of the system will eventually be determined by the collective velocity distribution. The observed correlation of the deformation of the flow distribution with that required for the non-spherical source may provide the physical explanation for the latter and thus serve as an additional justification for the present statistical approach. The significance of this work is, independently, derived from the consistent description of a large class of observables for conventionally selected central collisions. It demonstrates that the observed anisotropies do not necessarily imply the absence of equilibrium in the system. The constraining deformation parameters should be recovered from dynamical reaction models.

Acknowledgements

The authors would like to thank the staff of the GSI for providing high-quality ^{197}Au and ^{129}Xe beams and for technical support. Stimulating discussions with D.H.E. Gross and J.P. Wieleczko are gratefully acknowledged. This work has been supported by the European Community under Contract No. ERBFMG-ECT950083 and the CNRS-JINR Dubna agreement No 00-49, and by the IN2P3-CNRS, the DAPNIA/SPhN-CEA and the Regional Council of Basse-Normandie for the construction of the INDRA detector. M.B. and C.Sc. acknowledge the financial support of the Deutsche Forschungsgemeinschaft under the Contract Nos. Be1634/1 and Schw510/2-1, respectively; D.Go. and C.Sf. acknowledge the receipt of Alexander-von-Humboldt fellowships.

References

[1] E. Suraud, D. Cussol, Ch. Grégoire, D. Boilley, M. Pi, P. Schuck, B. Remaud, F. Sébille, Nucl. Phys. A **495** (1989) 73.

[2] J. Aichelin, Phys. Rep. **202** (1991) 233.

[3] G. Peilert, H. Stöcker, W. Greiner, Rep. Prog. Phys. **57** (1994) 533.

[4] P. Danielewicz, Phys. Rev. C **51** (1995) 716.

[5] D.R. Bowman *et al.*, Phys. Rev. Lett. **67** (1991) 1527; Phys. Rev. C **46** (1992) 1834.

[6] For recent reviews of the field see, e.g., *Proceedings of the International Workshop XXVII on Gross Properties of Nuclei and Nuclear Excitations*, Hirschegg, Austria, 1999, ed. by H. Feldmeier *et al.* (GSI, Darmstadt, 1999); D. Durand, E. Suraud, B. Tamain, *Nuclear Dynamics in the Nucleonic Regime*, ISBN 0750305371 (Institute of Physics, Bristol and Philadelphia, 2001).

[7] Bao-An Li, S.J. Yennello, Phys. Rev. C **52** (1995) 1746.

[8] H. Johnston *et al.*, Phys. Lett. B **371** (1996) 186.

[9] R. Nebauer, J. Aichelin and the INDRA Collaboration, Nucl. Phys. A **658** (1999) 67.

[10] F. Rami *et al.*, Phys. Rev. Lett. **84** (2000) 1120.

[11] D.H.E. Gross, Rep. Prog. Phys. **53** (1990) 605.

[12] J. Bondorf *et al.*, Phys. Rep. **257** (1995) 133.

[13] A. Schüttauf *et al.*, Nucl. Phys. A **607** (1996) 457.

[14] L. Beaulieu *et al.*, Phys. Rev. C **64** (2001) 064604.

[15] S.P. Avdeyev *et al.*, Nucl. Phys. A **709** (2002) 392.

[16] A. Le Fèvre, M. Płoszajczak, V.D. Toneev, Phys. Rev. C **60** (1999) 051602.

[17] B. Bouriquet *et al.*, in *Proceedings of the $XXXIX^{th}$ International Winter Meeting on Nuclear Physics*, Bormio, Italy, 2001, ed. by I. Iori, A. Moroni, Ricerca Scientifica ed Educazione Permanente Suppl. # 117 (Milano 2001), p. 84.

[18] F. Lavaud, E. Plagnol *et al.*, *Proc. of the Int. Nucl. Phys. Conf. INPC2001*, Berkeley CA, USA, 2001, ed. by E. Norman, L. Schroeder, G. Wozniak, AIP Conference Proceedings (Melville, New York 2002), p. 716.

[19] M. D'Agostino *et al.*, Phys. Lett. B **368** (1996) 259.

[20] N. Marie *et al.*, Phys. Lett. B **391** (1997) 15.

[21] R. Bougault *et al.*, in *Proceedings of the $XXXV^{th}$ International Winter Meeting on Nuclear Physics*, Bormio, Italy, 1997, ed. by I. Iori, Ricerca Scientifica ed Educazione Permanente Suppl. # 110 (Milano 1997), p. 225.

[22] N. Marie *et al.*, Phys. Rev. C **58** (1998) 256.

[23] J.D. Frankland *et al.*, Nucl. Phys. A **689** (2001) 905; Nucl. Phys. A **689** (2001) 940.

[24] R. Nebauer, J. Aichelin, Nucl. Phys. A **650** (1999) 65.

[25] R.J. Charity, Phys. Rev. C **64** (2001) 064610.

[26] S.C. Jeong *et al.*, Phys. Rev. Lett. **72** (1994) 3468.

[27] J.C. Steckmeyer *et al.*, Phys. Rev. Lett. **76** (1996) 4895.

[28] Al.H. Raduta, Ad.R. Raduta, Phys. Rev. C **65** (2002) 054610.

[29] N. Bellaize *et al.*, Nucl. Phys. A **709** (2002) 367.

[30] D.H.E. Gross, K. Sneppen, Nucl. Phys. A **567** (1994) 317.

[31] M. Begemann-Blaich *et al.*, Phys. Rev. C **58** (1998) 1639.

[32] J. Łukasik *et al.*, Phys. Rev. C **55** (1997) 1906.

[33] D. Gourio *et al.*, Eur. Phys. J. A **7**, 245 (2000).

[34] E. Plagnol *et al.*, Phys. Rev. C **61** (2000) 014606.

[35] S. Hudan *et al.*, Phys. Rev. C **67** (2003) 064613.

[36] M. D'Agostino *et al.*, Phys. Lett. B **371** (1996) 175.

[37] M.J. Huang *et al.*, Phys. Rev. Lett. **78** (1997) 1648.

[38] M.B. Tsang *et al.*, Phys. Rev. Lett. **71** (1993) 1502.

[39] W.C. Hsi *et al.*, Phys. Rev. Lett. **73** (1994) 3367.

[40] W. Reisdorf *et al.*, Nucl. Phys. A **612** (1997) 493.

[41] J. Łukasik *et al.*, Phys. Rev. C **66** (2002) 064606.

[42] J. Łukasik *et al.*, Phys. Lett. B **566** (2003) 76.

[43] F. Lavaud, Ph.D. Thesis, Université Louis Pasteur Strasbourg I, Report IPNO-T.01-06 (2001); F. Lavaud *et al.*, to be published.

[44] J. Pouthas *et al.*, Nucl. Inst. and Meth. in Phys. Res. A **357** (1995) 418.

[45] J. Pouthas *et al.*, Nucl. Inst. and Meth. in Phys. Res. A **369** (1996) 222.

[46] N. Marie, Ph.D. Thesis, Université de Caen, 1995, Report GANIL T 95 04.

[47] A. Trzciński *et al.*, Nucl. Inst. and Meth. in Phys. Res. A **501** (2003) 367.

[48] M. Pârlog *et al.*, Nucl. Inst. and Meth. in Phys. Res. A **482** (2002) 693.

[49] F. Hubert, R. Bimbot, H. Gauvin, Atomic Data Nucl. Data Tables **46** (1990) 1.

[50] C. Cavata *et al.*, Phys. Rev. C **42** (1990) 1760.

[51] O. Schapiro, D.H.E. Gross, Nucl. Phys. A **573** (1994) 143.

[52] O. Schapiro, D.H.E. Gross, Nucl. Phys. A **576** (1994) 428.

[53] J.C. Steckmeyer *et al.*, Nucl. Phys. A **686** (2001) 537.

[54] M.B. Tsang *et al.*, Phys. Rev. C **44** (1991) 2065.

[55] K. Morawetz, M. Płoszajczak, V.D. Toneev, Phys. Rev. C **62** (2000) 064602.

[56] J. Cugnon, D. L'Hôte, Nucl. Phys. A **397** (1983) 519.

[57] A. Bohr, B.R. Mottelson, *Nuclear Structure* (Benjamin, New-York, 1975), Vol. 2.

[58] A.S. Botvina, I.M. Mishustin, Phys. Rev. C **63** (2001) 061601.

[59] G.J. Kunde *et al.*, Phys. Rev. Lett. **74** (1995) 38.

[60] S. Pal, S.K. Samaddar, J.N. De, Nucl. Phys. A **608** (1996) 49.

[61] S. Chikazumi, T. Maruyama, K. Niita, A. Iwamoto, Phys. Lett. B **476** (2000) 273.

[62] C.B. Das, S. Das Gupta, Phys. Rev. C **64** (2001) 041601.

[63] F. Gulminelli, Ph. Chomaz, preprint nucl-th/0209032.

[64] X. Campi, H. Krivine, E. Plagnol, N. Sator, Phys. Rev. C **67** (2003) 044610.

[65] P. Danielewicz, Q. Pan, Phys. Rev. C **46** (1992) 2002.

[66] C.O. Dorso, J. Aichelin, Phys. Lett. B **345** (1995) 197.

[67] H.W. Barz *et al.*, Phys. Lett. B **382** (1996) 343.

[68] R.K. Puri *et al.*, Phys. Rev. C **54** (1996) 28.

[69] K.S. Lee, U. Heinz, E. Schnedermann, Z. Phys. C **48** (1990) 525.

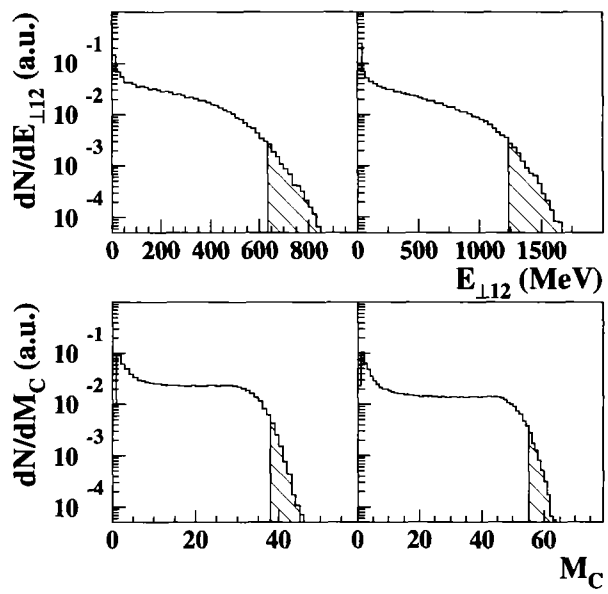

Fig. 1. Top panels: Distributions of the total transverse energy of light charged particles ($Z \leq 2$) for the reactions ^{129}Xe+^{nat}Sn at 50 A MeV (left) and ^{197}Au+^{197}Au at 60 A MeV (right). The hatched areas indicate central events with $b/b_{max} \leq 0.1$ selected according to this observable ($E_{\perp}^{12} \geq 637$ MeV and $E_{\perp}^{12} \geq 1256$ MeV, respectively). Bottom panels: Corresponding distributions of charged particle multiplicity M_c for the same two reactions. The reduced impact parameter $b/b_{max} \leq 0.1$ corresponds to $M_c \geq 38$ and $M_c \geq 55$, respectively (hatched areas).

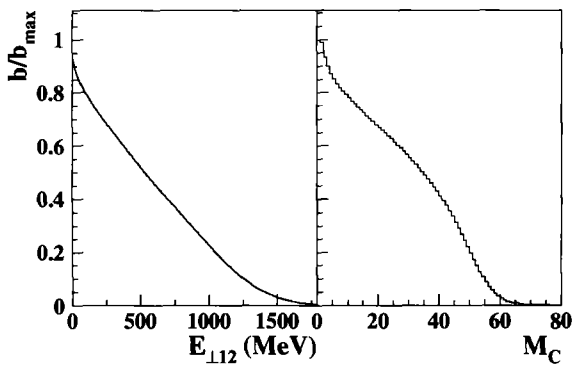

Fig. 2. Reduced impact parameter b/b_{max} as a function of the total transverse energy of light charged particles with $Z \leq 2$ (left) and of the multiplicity of charged particles (right) for the reaction ^{197}Au+^{197}Au at 60 A MeV. The trigger condition of at least three hits is only partially reflected in M_c because hits may be generated also by gamma rays and neutrons.

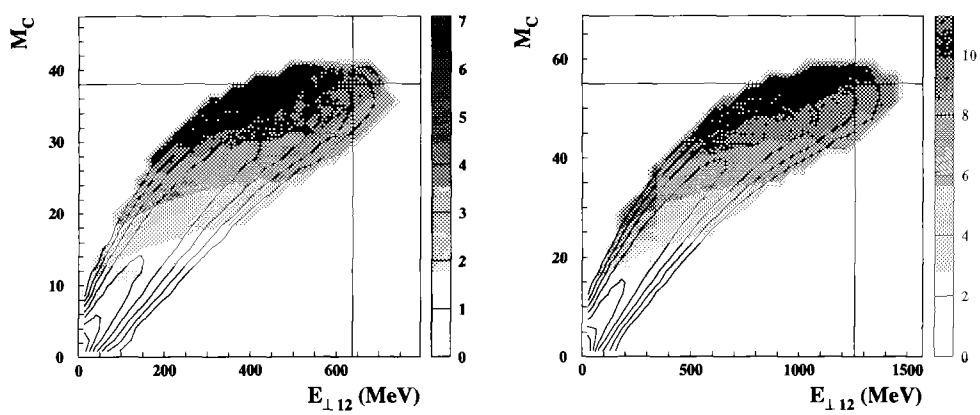

Fig. 3. Double-differential reaction cross section (logarithmic contour lines) and mean multiplicity of fragments with $Z > 2$ (shadings) as functions of the multiplicity of charged particles M_c and the total transverse energy $E_\perp^{12}$ of light charged particles ($Z \leq 2$) for ^{129}Xe+^{nat}Sn collisions at 50 A MeV (left) and ^{197}Au+^{197}Au at 60 A MeV (right). The horizontal and vertical lines indicate the minimum values of M_c and $E_\perp^{12}$ that have been used to select central events in these reactions.

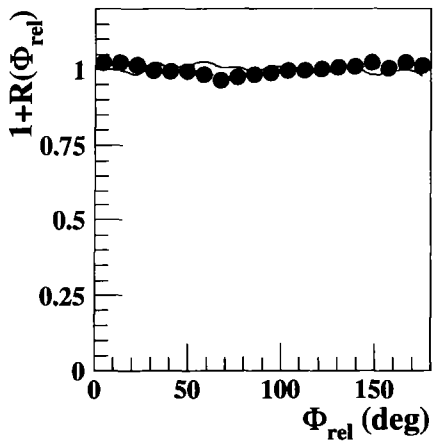

Fig. 4. Correlation functions in relative azimuthal angle between alpha particles. The symbols are the experimental data for central ^{129}Xe+^{nat}Sn collisions at 50 A MeV and the line represents the MMMC-NS model prediction with 40 $\hbar$ angular momentum.

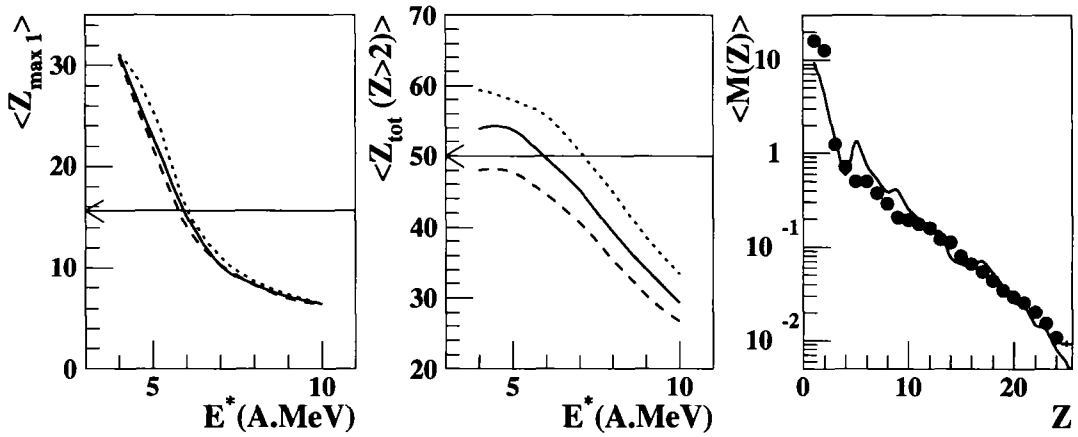

Fig. 5. Left: Mean value of the largest fragment charge within an event (Z_{max1}) as a function of the excitation energy for MMMC-NS predictions with different source size: $Z_{\mathrm{S}} = 70$ (dashed line), $Z_{\mathrm{S}} = 79$ (full line) and $Z_{\mathrm{S}} = 90$ (dotted line). The arrow points to the experimental value for central ^{129}Xe+$^{\mathrm{nat}}$Sn at 50 A MeV selected using $\mathrm{E}_{\perp}^{12}$. Middle: Mean total charge of fragments ($Z > 2$) for the same sources as in the left panel and the experimental value for the same reaction. Right: Mean measured multiplicity of fragments with charge Z (circles). The line is the MMMC-NS prediction with the source size $Z_{\mathrm{S}} = 79$ and excitation energy $E^* = 6$ A MeV. In all cases, only events having a detected total charge $Z_{\mathrm{tot}} \geq 80\%$ of the initial system charge have been included.

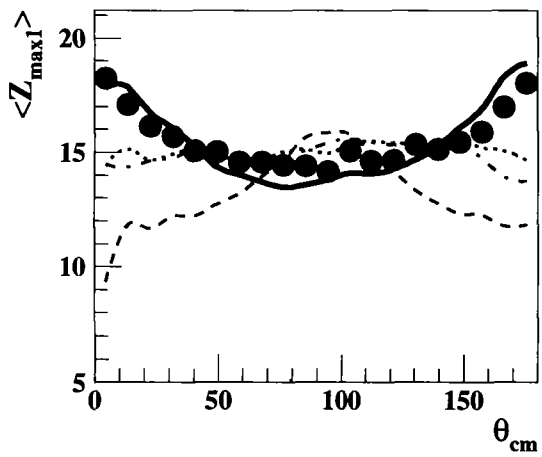

Fig. 6. Mean measured value of the largest fragment charge within an event (Z_{max1}) as a function of the polar angle in the center-of-mass, θ_{cm}, for central collisions of ^{129}Xe+$^{\mathrm{nat}}$Sn at 50 A MeV selected using $E_{\perp}^{12}$ (circles) with the requirement $Z_{\mathrm{tot}} \geq 80\%$. MMMC-NS model predictions are given for a prolate (full line), a spherical (dotted) and an oblate (dashed) source, and for a spherical source with non-isotropic radial flow (dashed-dotted line).

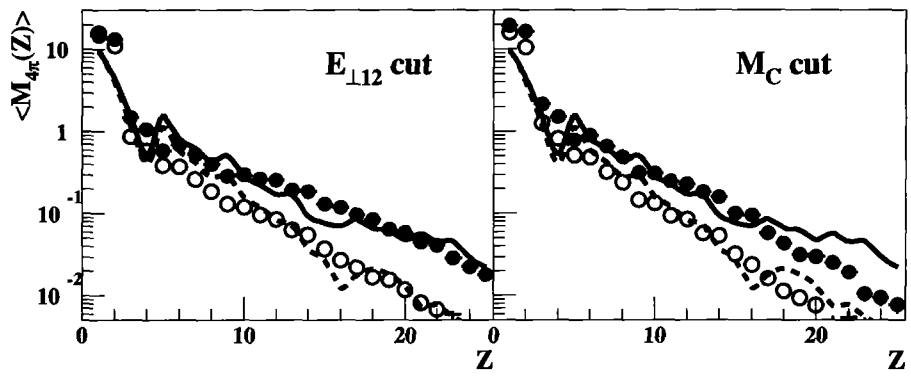

Fig. 7. Mean multiplicity of fragment charges, normalized to a solid angle of 4π, with selection of central events using $E_{\perp}^{12}$ (left panel) and M_c (right). The circles represent the experimental data for central ^{129}Xe+^{nat}Sn collisions at 50 A MeV and the lines are the MMMC-NS predictions with the prolate source. Full symbols and solid lines represent the results for forward angles ($\theta_{cm} \leq 60°$), open symbols and dashed lines for sideward angles ($60° < \theta_{cm} \leq 120°$). Experimental error bars are smaller than the symbol size.

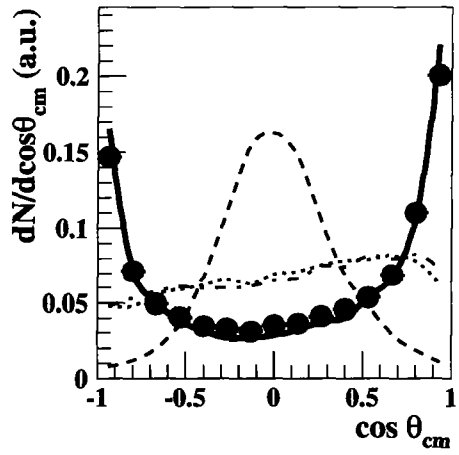

Fig. 8. Angular distribution of the largest fragment (Z_{max1}) within an event. Experimental data for central ^{129}Xe+^{nat}Sn collisions at 50 A MeV (circles) and MMMC-NS predictions after filtering for the prolate (full line), spherical (dotted) and oblate (dashed) sources, and for the spherical source with non-isotropic flow (dashed-dotted). All distributions are normalized to the same area. The forward-backward asymmetry is caused by the experimental acceptance.

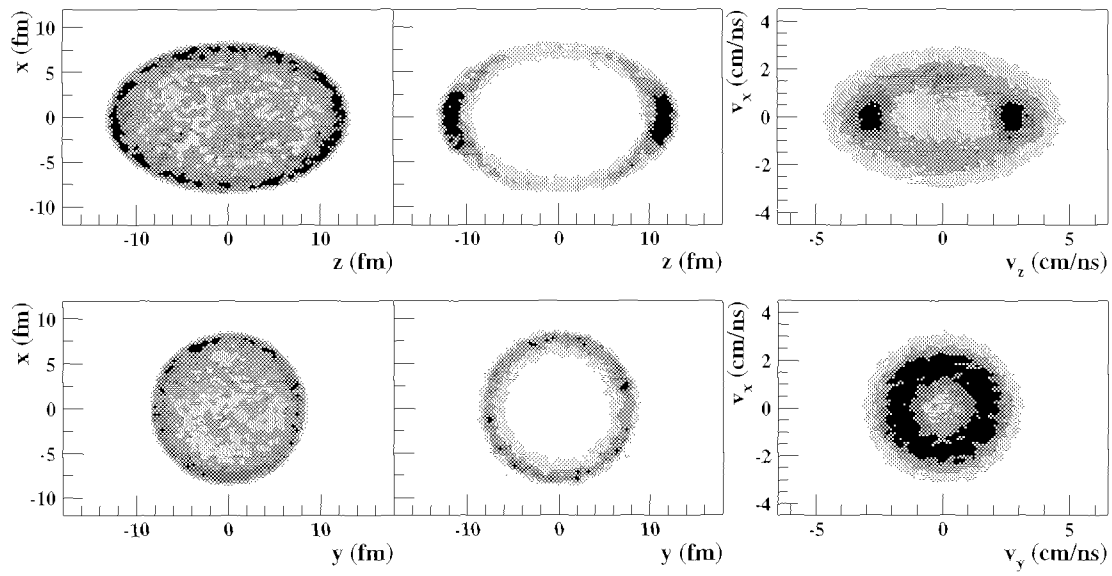

Fig. 9. Two-dimensional distributions of fragments with $Z > 4$, calculated in the MMMC-NS model with the prolate source and before filtering, in coordinate space without Coulomb interaction (left), with Coulomb interaction (center) and in velocity space with Coulomb interaction (right). The top panels show the projections within a centered longitudinal slice with widths 5 fm and 2 cm/ns in space and velocity, respectively. The bottom panels show the corresponding projections, for transversal slices with the same thickness. The z-axis is oriented in the beam direction, the shading scale is linear.

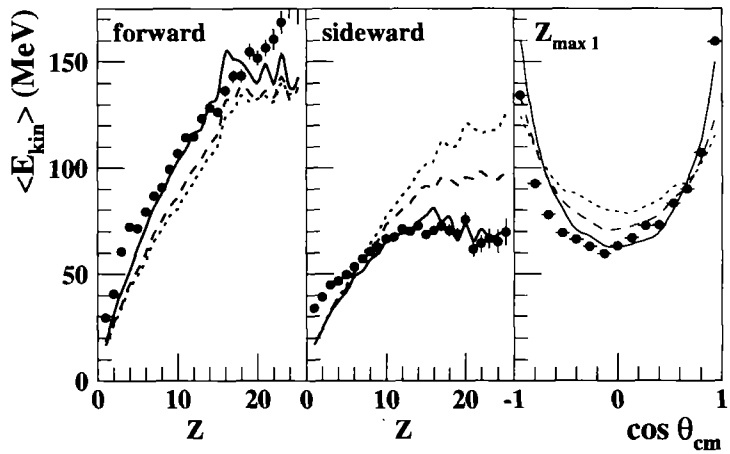

Fig. 10. Left: Mean kinetic energy of fragments in the center-of-mass as a function of Z at forward angles ($\theta_{cm} \leq 60°$), calculated within the MMMC-NS model and after filtering, for the prolate source with scaling exponents $\alpha_{coll} = 0.5$ (dotted), 1 (dashed) and 2 (full lines). The symbols represent the experimental data for central ^{129}Xe+^{nat}Sn collisions at 50 A MeV. Middle: The same as in the left panel but for sideward angles ($60° < \theta_{cm} \leq 120°$). Right: The mean kinetic energy in the center of mass of the largest fragment (Z_{max1}) as a function of the emission angle.

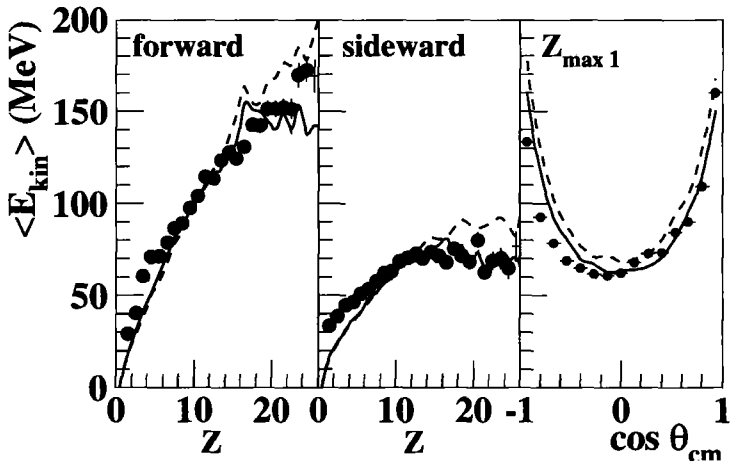

Fig. 11. Mean kinetic energy of fragments in the center-of-mass for central ^{129}Xe+^{nat}Sn collisions at 50 A MeV in the representation of Fig. 10. The symbols represent the experimental data and the full lines are the MMMC-NS model results for the prolate source with isotropic flow and $\alpha_{coll} = 2$, as shown in Fig. 10. The dashed lines represent the results for the prolate source with non-isotropic flow of elongation 0.70:1.

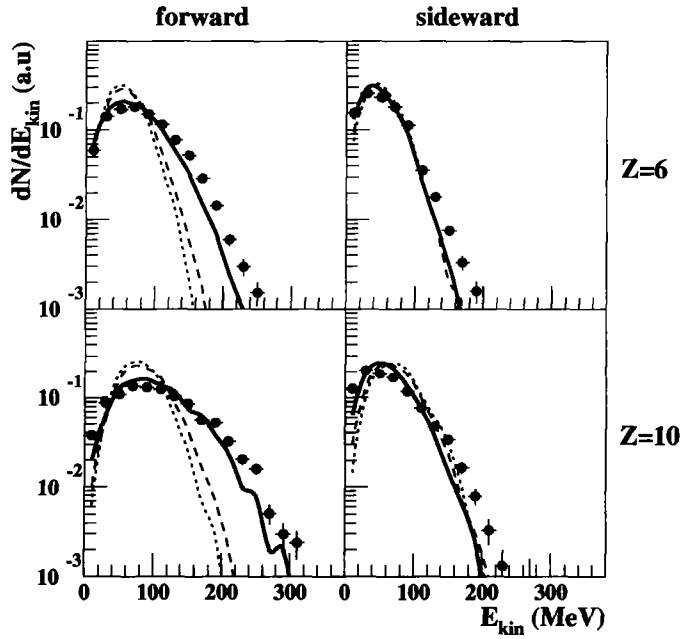

Fig. 12. Kinetic energy spectra (in the center of mass) of fragments with $Z = 6$ (top) and $Z = 10$ (bottom) at forward angles (left panels) and at sideward angles (right panels). The circles are the experimental data for central ^{129}Xe+^{nat}Sn collisions at 50 A MeV. The lines represent MMMC-NS predictions for the prolate source with scaling exponents $\alpha_{coll} = 0.5$ (dotted lines), 1 (dashed lines) and 2 (full lines).

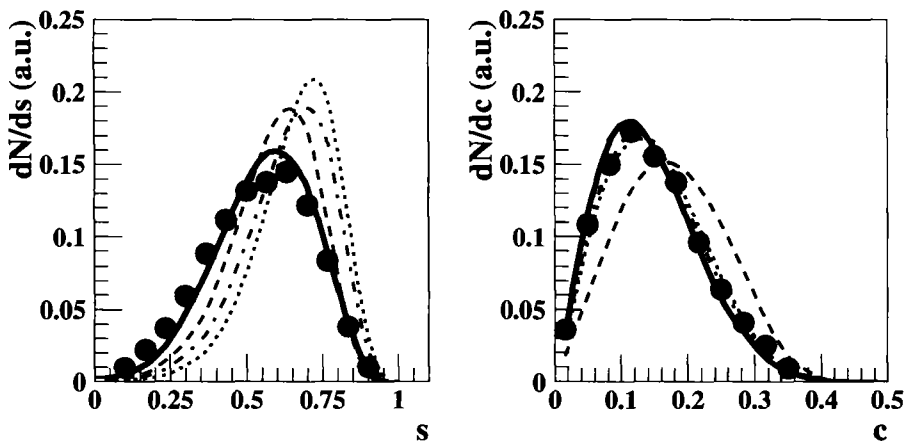

Fig. 13. Sphericity (left panel) and coplanarity (right panel) distributions. The circles represent the experimental data for central ^{129}Xe+^{nat}Sn collisions at 50 A MeV and the lines are the MMMC-NS model predictions for the prolate (full line), spherical (dotted) and oblate (dashed) sources and for the spherical source with non-isotropic flow (dashed-dotted). The distributions are normalized to the same area.

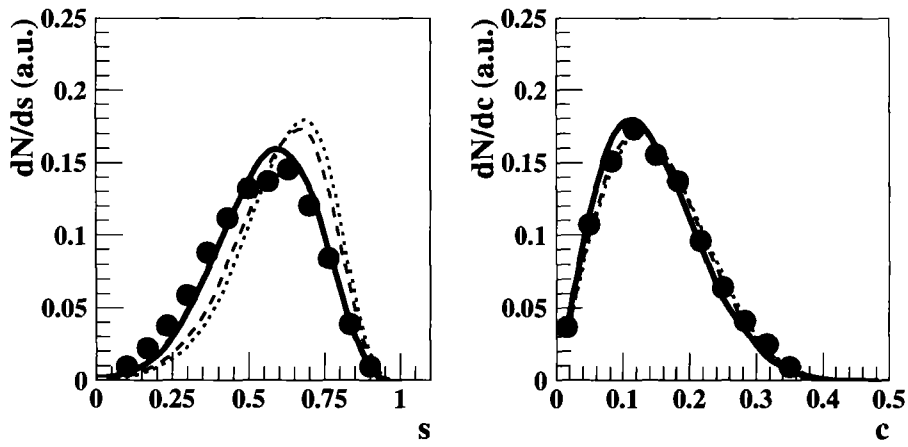

Fig. 14. Sphericity (left panel) and coplanarity (right panel) distributions compared to MMMC-NS model predictions for the prolate source with exponents of the flow profile $\alpha_{coll} = 0.5$ (dotted), 1 (dashed) and 2 (full lines).

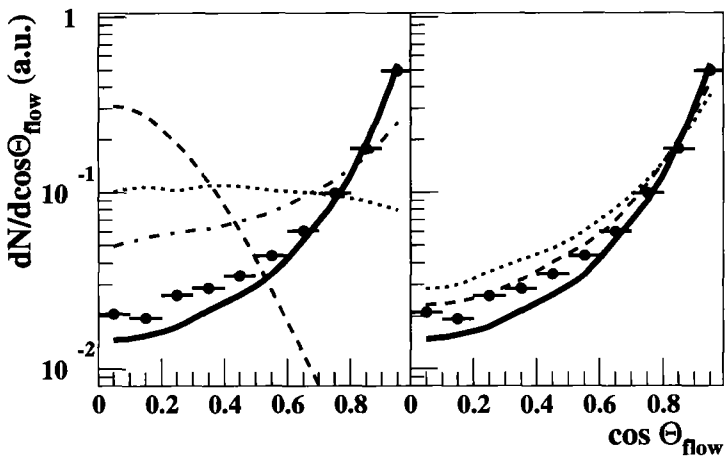

Fig. 15. Flow angle distributions: Experimental data for central ^{129}Xe+^{nat}Sn collisions at 50 A MeV (full circles) and MMMC-NS model predictions (lines) for different source shapes (left panel, notation as in Fig. 6), and for the prolate source with different exponents α_{coll} = 0.5 (dotted), 1 (dashed) and 2 (full lines) of the flow profile (right panel). The distributions are normalized to the same area.

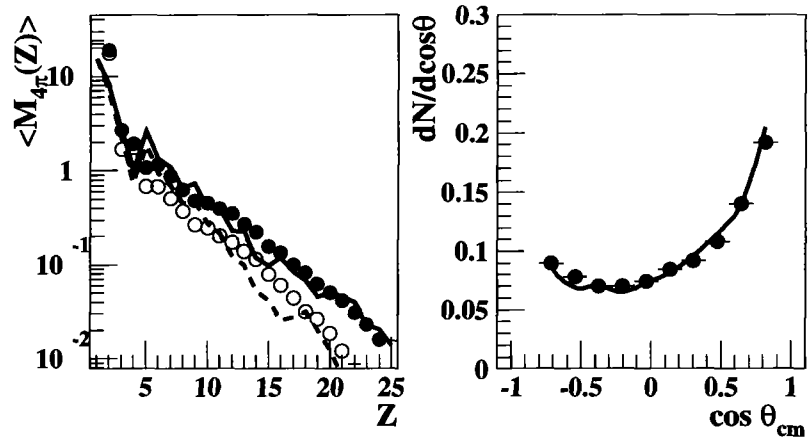

Fig. 16. Left: Mean multiplicity of fragment charges, normalized to a solid angle of 4π, with selection of central events using $E_{\perp}^{12}$. The circles represent the experimental data for central ^{197}Au+^{197}Au collisions at 60 A MeV, and the lines are the MMMC-NS model predictions calculated for the prolate source with parameters given in Table 3. The full circles and the solid line correspond to forward angles, the open circles and the dashed line correspond to sideward angles. Right: Angular distribution of the largest fragment (Z_{max1}) within an event for the same reaction. The full circles and the solid line represent the experimental data and the MMMC-NS model predictions, respectively. The distributions are normalized to the same area, the forward-backward asymmetry is caused by the experimental acceptance.

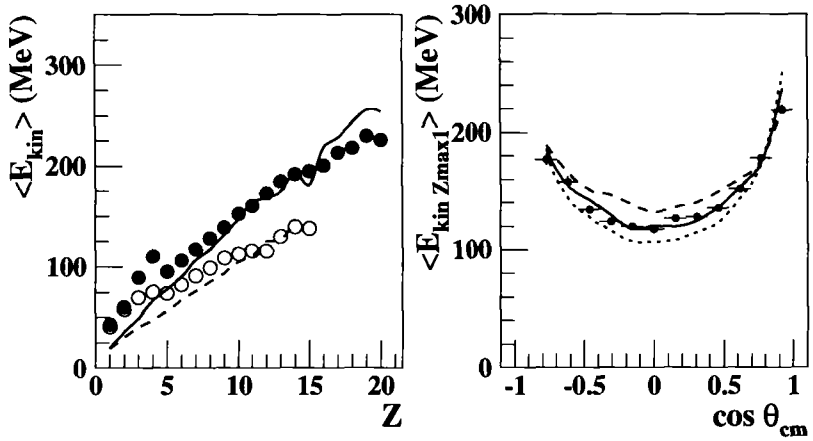

Fig. 17. Left: Mean fragment kinetic energy as a function of Z in the center-of-mass system. The circles are experimental data for central ^{197}Au+^{197}Au collisions at 60 A MeV and the lines are the corresponding MMMC-NS prolate-source predictions for forward (full circles and solid line) and sideward angles (open circles and dashed line). Right: Mean kinetic energy in the center of mass for the largest fragment (Z_{max1}) as a function of the angle; the circles are the experimental data, the dotted, full and dashed lines represent the MMMC-NS prolate-source predictions with $\alpha_{\mathrm{coll}} = 1$, 1.5 and 2, respectively.

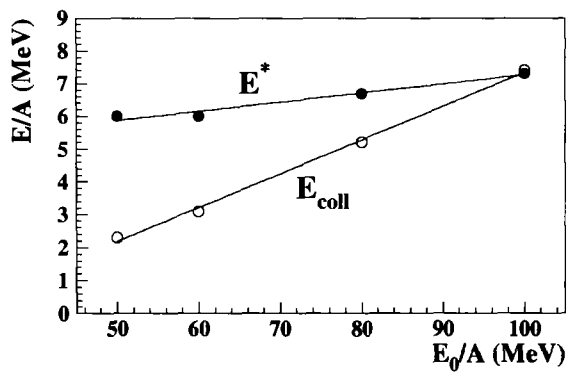

Fig. 18. Mean thermal excitation energy (full circles) and collective flow energy (open circles) at freeze-out, extracted by means of the MMMC-NS model, as a function of the incident energy E_0/A for central collisions of ^{129}Xe+$^{\mathrm{nat}}$Sn at 50 A MeV and ^{197}Au+^{197}Au at 60, 80 and 100 A MeV. The lines are linear fits, meant to guide the eye.

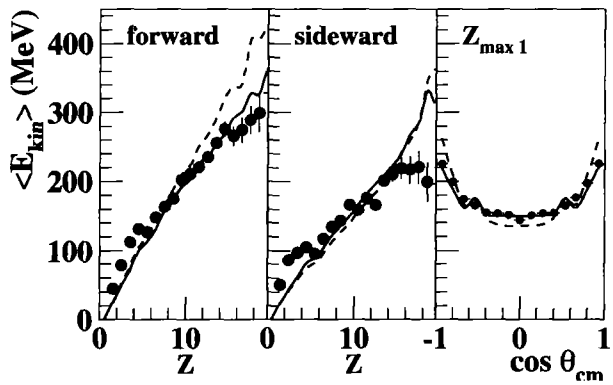

Fig. 19. Mean kinetic energy of fragments in the center-of-mass for central ^{197}Au+^{197}Au collisions at 100 A MeV in the representation of Fig. 11. The symbols represent the experimental data and the full lines are the MMMC-NS model results for the prolate source with isotropic flow and $\alpha_{\rm coll} = 1.2$, the dashed lines represent the results for the prolate source with non-isotropic flow of elongation 0.76:1.